

Deep Learning-Optimized Acoustic Metamaterial for Sound Energy Harvesting

Ziyao Xiong, Yucheng (Kevin) Ni, Xinyue (Alina) Zhang

I. AIMS AND RESEARCH SUMMARY

THIS project addresses the dual challenges of energy scarcity and noise pollution by harnessing sound energy as a renewable resource, offering a sustainable alternative to fossil fuels, which significantly contribute to global carbon emissions. Although sound energy is abundant, it remains underutilized, particularly in subway systems where consistent train noise can serve as a reliable energy source. Noise pollution, associated with increased cardiovascular risks at prolonged exposure above 55 dB [1], can exceed 120 dB in subways [2], leading to over 3,000 noise complaints despite Transport for London (TfL) spending £150 million annually on track maintenance [3]. To tackle this, we developed an acoustic metamaterial structure that absorbs incident noise when applied to subway tunnel walls. Our solution, estimated to cost £9 million for full implementation across the London Underground, not only mitigates noise pollution but also converts the absorbed noise into usable electrical energy.

Our development process began with measuring the subway noise spectrum. Leveraging deep learning algorithms and topological optimization, we designed the geometric structure and material properties of the acoustic metamaterials to create the desired bandgap. The final device integrates perforated plates and piezoelectric membranes with the designed crystal structure, achieving up to 95% noise absorption, an overall absorption efficiency of 80%, and converting the absorbed noise into electrical signals exceeding 2.5V.

II. DETAILED DESCRIPTION AND ANALYSIS OF FINDINGS

A. Analysis of underground noise spectrum

To design a metamaterial can absorbing underground noise and converting it into energy, a comprehensive frequency analysis is essential. We recorded the noise produced by an underground train through an open cabin window, as this better captures the relevant frequencies for a tunnel-exterior application. The time-domain data was processed using a Fourier Transform in Python to convert it into the frequency domain. The spectrum exhibits significant fluctuations, primarily due to irregularities in the recorded signal, and the inherent randomness of the noise source. Smoothing the frequency spectrum is therefore applied to mitigate these fluctuations, enhancing the visibility of meaningful frequency components and reducing the impact of noise. In this study, we employ 1/3 octave smoothing, which groups frequencies into logarithmically spaced bands (octaves) and averages the values within each band [4]. This method reflects how human perception processes sound and is commonly used in acoustic analysis. This technique is especially beneficial in identifying dominant noise frequencies that the metamaterial structure will need to target

for energy conversion. The spectrum after octaves smoothing is shown in Fig. 2.

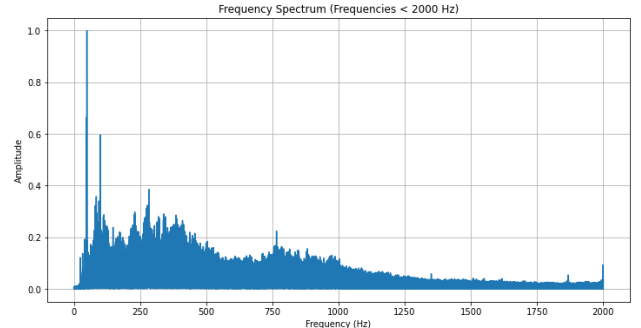


Fig. 1. Frequency spectrum of underground noise after FFT. The amplitude of frequencies greater than 2000 Hz is generally below 0.1, indicating that they do not exhibit typical behavior and are therefore excluded from further analysis. Despite the presence of some fluctuations, the general trend of the frequency spectrum remains clear.

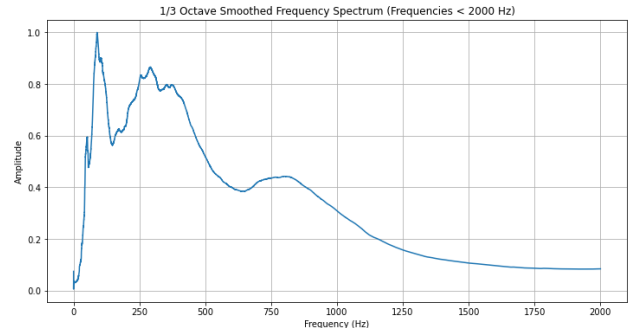


Fig. 2. Frequency spectrum of underground noise after octaves smoothing. Peaks can be clearly identified.

We identified three prominent peaks in the frequency spectrum, approximately centered at 90 Hz, 315 Hz, and 850 Hz. The first peak is relatively narrow, spanning only about 70 Hz, while the other two are significantly broader, each covering a range of approximately 300 Hz. Our objective is to design a metamaterial structure that effectively targets and maximizes absorption at these frequency peaks, as they represent the dominant noise components critical for energy conversion.

B. Acoustic Metamaterial

The concept of metamaterials was first introduced within the framework of left-handed materials [5], initially as theoretical models. The first practical metamaterial was developed using split-ring resonators to achieve negative magnetic permeability [6], demonstrating properties not found in nature. This led to the term "metamaterial" for materials with extraordinary physical characteristics. Research has since expanded to include acoustics [7], where acoustic metamaterials manipulate sound at sub-wavelength scales [8], enabling effects like lossless transmission [9] and acoustic cloaking [10]. Based on local resonance [11], these materials can be modeled as spring-mass systems, and when arranged periodically, they resemble phononic crystals, as

shown in Fig. 3. Two key traits of phononic crystals are valuable in our research. Firstly, local resonance enables sub-wavelength sound absorption [12], ideal for addressing low-frequency noise where traditional materials like foam are ineffective without excessive thickness [13]. Other methods like destructive interference are also impractical due to the long wavelengths of low-frequency noise, requiring large devices. Acoustic metamaterials, through local resonance, absorb and dissipate sound energy efficiently [14]. Secondly, phononic crystals can concentrate energy. Introducing defects into the periodic structure, as shown in Fig. 3, localizes mechanical waves at specific frequencies around the defects [15], forming defect states that enhance energy density, enabling efficient energy harvesting.

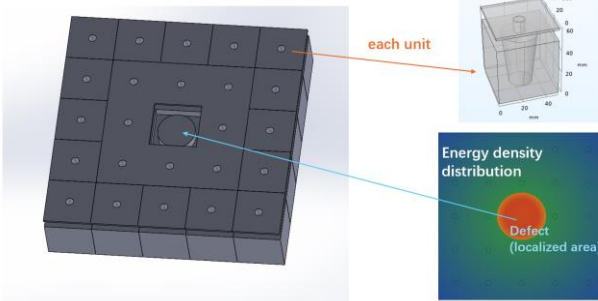


Fig. 3. Phononic crystal units arranged in a square lattice. When the local resonance occurs, the energy becomes concentrated at the center, resulting in a radially distributed energy density pattern emanating from the center.

Achieving superior sound absorption and energy capture is our goal, and both properties can be attained by analyzing the bandgaps of phononic crystals through lattice theory [16]. Bandgap is a specific frequency range that sound waves cannot propagate through the material. Local resonance induces low-frequency bandgaps, with defect states appearing within these gaps [17].

To compute the band gaps of acoustic metamaterials, the finite element method (FEM) is employed in COMSOL Multiphysics. Due to the complexity and time requirements of 3D simulations, 2D simulations are used. A typical 2D metamatereial structure, shown in Fig. 4, consists of scattering bodies designed to scatter, reflect, or refract waves, creating band gaps where certain frequencies are blocked. The substrate, typically air, supports wave propagation and enhances control of airborne sound in tunnels. An air substrate is crucial for efficient wave interaction, as a solid substrate would not interact effectively with airborne sound.

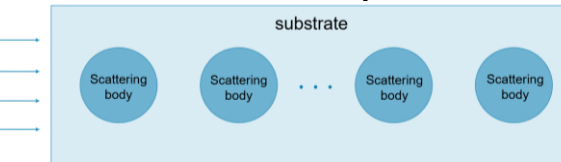


Fig. 4. A 2D periodically arranged phononic crystal with substrate and circular scattering bodies.

In a periodic medium, the displacement field $u(r)$, which represents the wave function at a position r , exhibits periodicity in accordance with the underlying lattice structure. Specifically, for a lattice period R , the displacement field $u(r)$ satisfies the Bloch's boundary condition:

$$u(r + R) = u(r)e^{ik \cdot R}. \quad (1)$$

Here, k represents the wave vector, and the phase factor $e^{ik \cdot R}$ accounts for the difference in phase as the wave function propagates through the periodic structure. This relationship indicates that the wave function repeats its form at each lattice site, differing only by a phase shift dependent on the wave vector and the lattice translation vector.

The wave equation satisfies the differential equation:

$$\nabla \cdot [\mu(r) \nabla u(r)] + \nabla \cdot [\lambda(r) \nabla \cdot u(r)] = -\rho(r) \omega^2 u(r), \quad (2)$$

where $\rho(r)$ is the material density, $\lambda(r)$ and $\mu(r)$ are the Lame constants. Next, using FEM, we discretize the domain into small elements, as shown in Fig. 5(a), and approximate the displacement field as a sum of shape functions over nodal degrees of freedom:

$$u(r) \approx \sum_i N_i(r) u_i, \quad (3)$$

where N represents a shape function.

In periodic structures, a key boundary condition is the continuity of the displacement field at the edges of each material in the structure. This ensures that the displacement fields remain physically consistent across adjacent cells in the periodic medium. Additionally, Bloch boundary conditions, expressed in equation (1), are applied, linking the displacement fields between different periodic cells. Upon solving equation (2) in each mesh element, the bandgap computation is then framed as an eigenvalue problem:

$$(\mathbf{K} - \omega^2 \mathbf{M}) \mathbf{U} = 0, \quad (4)$$

where \mathbf{K} is the stiffness matrix, \mathbf{M} is the mass matrix, ω is the angular frequency, and \mathbf{U} is the displacement vector. The solutions of ω represent the propagating frequencies. If certain ω values are absent for all k directions, a band gap exists. Solving for all k in 2D is impractical, so we use the Brillouin Zone, which condenses essential wavevector information. In a square lattice as per Fig. 5(b), the irreducible Brillouin Zone further simplifies computations by restricting analysis to a small triangular section, mirrored via symmetry. Since band gaps occur along paths between high-symmetry points, analyzing only the edges suffices for band gap identification [18].

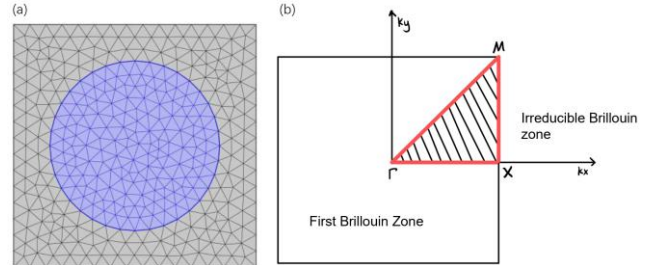


Fig. 5(a). Mesh of one cell for computing FEM. (b). Illustration of first Brillouin zone and irreducible Brillouin zone, high-symmetry points are Γ , X , and M . The analysis only needs to be done along the red line.

The stiffness matrix arises from the discretization of the elastic strain energy and depends on elasticity modulus and Poisson's ratio. The mass matrix is derived from the kinetic energy and depends on material density and geometry. Thus, band gaps can be identified based on the material's Poisson's ratio, elasticity modulus, density, and geometry.

Conventional bandgap design methods, such as trial-and-error, can be time-consuming and computationally expensive. To address this challenge, we introduce deep learning to assist in the design process. There exists a projection relationship between the characteristic parameters of acoustic metamaterials and their bandgaps. By constructing an appropriate deep learning model, we can achieve forward predictions of metamaterial properties, significantly enhancing the efficiency and accuracy of the design process.

C. Design of metamaterial structure with deep learning

1) Dataset generation

Our goal is to find a structure with a band gap that matches the measured peak frequency of underground noise. To achieve this, we aim to train a machine learning model capable of generating the desired structure and parameters.

The first step in training the machine learning model is to generate a dataset by randomly selecting material parameters for the scattering body. Using the NumPy.Random function in Python, we generate 100 sets of parameters, including Poisson's ratio, elasticity modulus, and density, within practical ranges. Since we focus on low-frequency sound manipulation, soft materials are preferred for the scattering body [19]. Thus, we generate the elasticity modulus within the range of 1 to 20 MPa, Poisson's ratio between 0.45 and 0.499, and density between 1.0 and 1.4 g/m³.

To generate different structural forms, topological configurations are employed to represent the basic units of metamaterials. Topological configuration refers to the spatial distribution of materials within a structure, providing a detailed description of the geometry and material composition [20]. The structure's spatial region is divided into grids, with each grid cell assigned a material, represented by a unit vector. The finer the grid, the more detailed the shape and material boundaries observed, but this comes at the cost of increased computational complexity. We chose a 25x25 grid to balance between grid refinement and computational load. However, the overall sample space is vast, and many configurations are impractical. Therefore, generation rules are applied to constrain the design of metamaterial topologies: i. For simplicity, the basic unit exhibits one-eighth symmetry. ii. To balance band gap presence and material usage, the scatterer body's filling ratio is constrained between 0.3 and 0.65. iii. Scatterers must form a single connected domain, ensuring that each scatterer grid cell has at least one neighboring scatterer cell. We generated 100 geometries, and some of them are shown in Fig. 6.

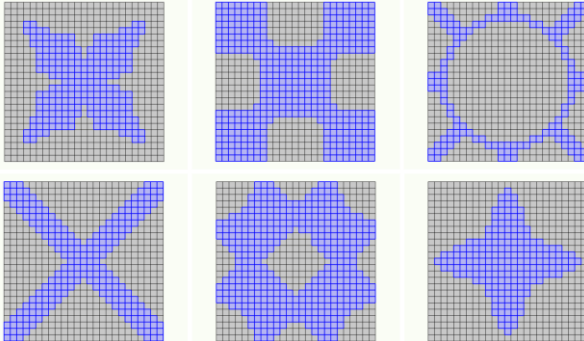


Fig. 6. The 2D geometries generated by Python based on the rules. The blue area represents the scatterers, and the grey area represents the substrates.

The topological model data is organized into grid structures representing material distribution within a metamaterial unit cell and stored in an Excel spreadsheet. A MATLAB script is then developed to automate data processing, assigning generated material properties to each scatterer, and formatting it for COMSOL Multiphysics. COMSOL with MATLAB is used to compute the band gaps for each configuration, with MATLAB automatically loading the datasets, running simulations, extracting results, and storing the band gap data in spreadsheets.

2) Forward prediction with MLP

We aim to train a model to predict the band gap of a given structure and material, which can be effectively achieved using an MLP in TensorFlow. A Multilayer Perceptron (MLP) is a feedforward neural network with multiple layers, where each neuron performs a weighted sum of its inputs followed by a non-linear ReLU activation function [21]. This allows the MLP to capture complex data patterns. Training involves feeding the model input data (material parameters and geometry) and target outputs (band gaps). The model

optimizes its weights using backpropagation and the Adam optimizer to minimize the Mean Squared Error (MSE) loss function for regression. After training, the MLP can instantly predict band gaps for new designs without needing COMSOL simulations. We will use this trained model in the next step.

3) Inverse prediction with VAE

In the metamaterial design process, the Variational Autoencoder (VAE) plays a key role by compressing high-dimensional topological structures into a set of latent variables through the encoder. These latent variables capture the essential features of the design while discarding redundant information. The decoder reconstructs the original structure from the latent variables, ensuring that key design information is preserved. The VAE is trained by minimizing a loss function, including Kullback-Leibler (KL) divergence [22], which ensures the latent variables follow a well-structured normal distribution. This allows for smooth interpolation between designs and ensures that generated latent variables correspond to valid designs.

Once trained, an inverse prediction network generates the desired design by searching the latent space for the latent variables that produce a specific target band gap. The inverse model starts with an initial guess and uses a forward prediction model to estimate the band gap, iteratively adjusting the latent variables via backpropagation until the predicted band gap matches the target. Once the error is minimized, the optimal latent variables are passed to the VAE's decoder to reconstruct the corresponding metamaterial design. This process is illustrated in Fig. 7.

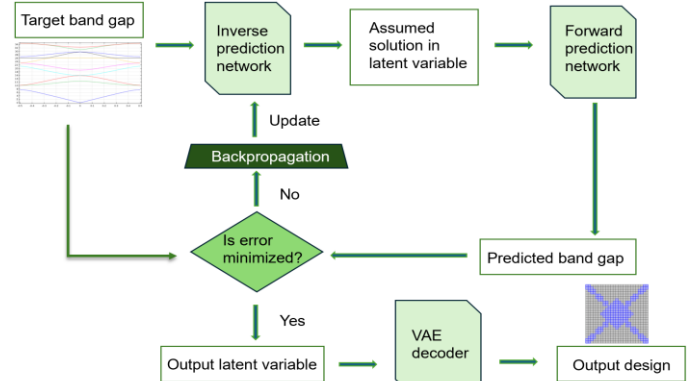


Fig. 7. A flowchart of the process of design of metamaterial using VAE.

4) Deep-learning results

The machine-learned material properties for the scattering body, with an elasticity modulus of 10 MPa, Poisson's ratio of 0.48, and density of 1.2 g/m³, indicate that the material closely resembles rubber. While the output metamaterial topology is initially in 2D, a 3D model is required.

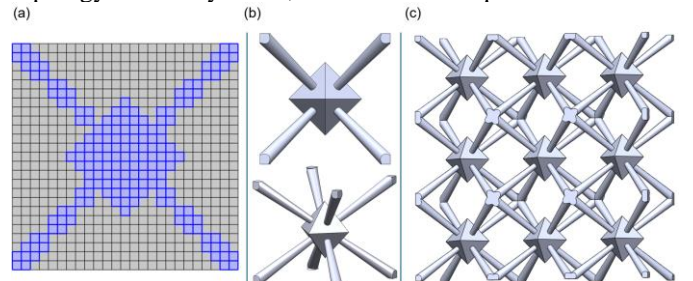


Fig. 8. (a) 2D projection of the model, output by deep learning; (b) a single 3D unit cell, designed to resemble the 2D projection from each direction; (c) the final structure formed by connecting multiple 3D unit cells.

We propose a method where the 3D model is designed to resemble the 2D topology when viewed from the x, y, and z directions, ensuring consistent wave behavior in all directions.

and achieving the desired 3D performance. The machine-designed 2D topology is shown in Fig. 8(a), the deduced 3D model in Fig. 8(b), and its periodic arrangement in Fig. 8(c). The bandgap of the final model was simulated and calculated in COMSOL, as shown in Fig. 9. The bandgap of the final model closely matched our intended region, corresponding to the peak of the noise spectrum observed in the underground.

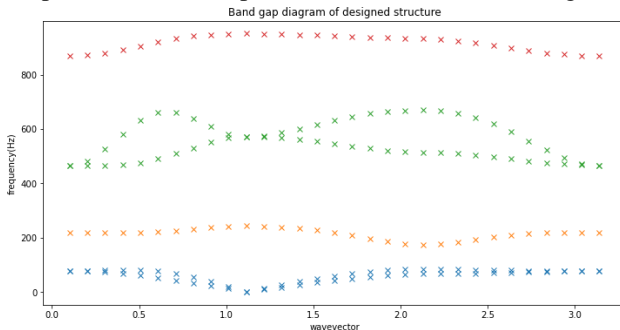


Fig. 9. Band gap diagram of final designed 3D structure. The band gaps clearly include noise peaks of 90 Hz, 315 Hz, 850 Hz.

D. Perforated plates

As mentioned earlier, local resonance can effectively absorb sound waves; however, the resonance frequencies are typically very narrow. We have designed these resonances to match the most prominent noise peaks. Nonetheless, noise also exists over a broader frequency range. To address this, we introduced perforated plate structures to enhance absorption across a wider frequency spectrum.

Inspired by the work of Li et al. [23], we integrated perforated plates into the crystal structure, converting enclosed positions within individual unit cells into Helmholtz resonators. This approach allows for the independent design of sound absorption capabilities without altering the mechanical properties of the crystal structure, such as its bandgap. By adjusting the diameter and depth of the perforations, the absorption frequency can be precisely controlled. We utilized COMSOL for numerical simulations to optimize these designs. As shown in Figure.10(a), the sound absorption simulation involves acoustic-solid coupling, incorporating both pressure acoustics and solid mechanics physics fields. The Perfectly Matched Layer (PML) is employed to minimize reflections from the simulation boundaries, ensuring that only the interactions within the crystal structure are analyzed accurately.

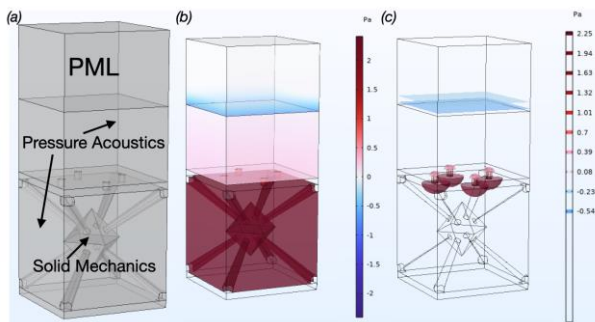


Fig. 10: (a) Absorption simulation in COMSOL with an applied incident pressure field. Pressure acoustic boundary conditions are used in the substrate (air), while solid mechanics boundary conditions are applied to the scattering body. (b) Sound pressure surface plot. PML has zero pressure. (c) Sound pressure isosurface at absorbable frequencies.

It is evident that the sound pressure inside the crystal structure is significantly higher than outside, indicating that the majority of the sound waves are absorbed by the device. This demonstrates the effective energy trapping and absorption capabilities.

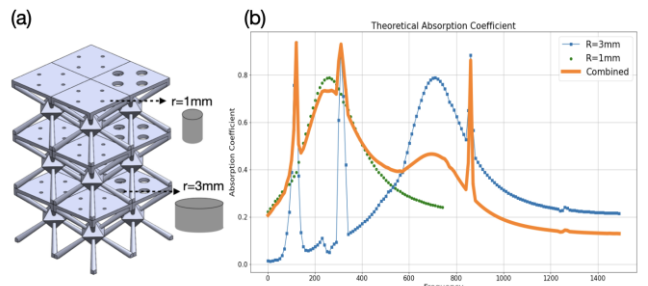


Fig.11 Heterogeneously assemble structure and its absorption coefficient

According to Cascading Resonator Theory [24], arranging Helmholtz resonators with varying resonance frequencies in series enhances sound absorption. By heterogeneously combining resonators, the full noise spectrum can be matched. Our simulations show that combining resonators with hole radii of 1mm and 3mm in a 3:1 ratio yields an absorption effect optimized for the noise spectrum.

E. Evaluation of absorption coefficient

The final step of our study is measuring how many waves our product can absorb. To achieve this, we utilize the transfer function method, which is well-suited for confined environments such as underground tunnels. The sound absorption coefficient (α) is calculated to quantify the material's effectiveness in absorbing sound, ranging from 0 to 1, higher the α , greater the material's performance on sound absorption. Using a controlled setup like an impedance tube prevents interference from reflections, ensuring accurate measurements [25]. As depicted in Fig. 3, the impedance tube generates plane acoustic waves, and by placing two microphones at known positions, we can capture the pressure at two points in the tube, $p_A(t)$ and $p_B(t)$. They are then transformed to the frequency domain, resulting in frequency signals $P_A(f)$ and $P_B(f)$. The transfer function H_{12} is then calculated from the ratio of the pressures measured:

$$H(f) = \frac{P_A(f)}{P_B(f)}. \quad (5)$$

Since and $P_A(f)$ and $P_B(f)$ are complex, $H(f)$ also contains both amplitude and phase information.

The reflection coefficient r can be obtained using the transfer function and wave propagation model:

$$R = \frac{H(\omega) - e^{-jks}}{1 - H(\omega)e^{-jks}}, \quad (6)$$

where $H(\omega)$ is the transfer function in the angular frequency domain, k is the wave number, and s is the distance between the microphones. The absorption coefficient α can be calculated from the reflection coefficient r as:

$$\alpha = 1 - |r|^2. \quad (7)$$

Commercially available impedance tubes, such as the Brüel & Kjær Type 4206 [26], exceed our budget, leading us to construct our own low-cost impedance tube. To design an impedance tube for measurements in the frequency range of 0 to 2000 Hz, four key quantities must be determined: the tube diameter d , microphone spacing s , the distance x_2 between the two microphones, and the length of tube 1. The tube diameter d is selected based on the upper frequency limit, ensuring that only plane waves propagate inside the tube [27]. For circular tubes, d is calculated using the formula:

$$d < 0.58 \frac{c}{f_u}, \quad (8)$$

where c is speed of sound and f_u is 2000Hz. Thus, we set the diameter of tube to be 9cm. The microphone spacing s must be chosen to avoid singular points where the reflection

coefficient r becomes indeterminate. As per Chung and Blaser's condition [28], s is governed by:

$$s < \frac{c}{2f_u}, \quad (9)$$

where we set s to be 4cm. Finally, the distance x_2 between the microphones and length of tube l must satisfy:

$$l - s - x_2 > 3d, \quad (10)$$

where we set l to be 40cm and x_2 to be 7cm.

To construct the impedance tube, we used PVC pipes for their affordability and smooth internal surfaces, ensuring proper sound wave propagation. A speaker at one end generates sound waves, and two sound card microphones are positioned at precise intervals to capture the sound pressure signals. We developed a MATLAB program to control the loudspeaker, performing a frequency sweep from 0 to 2000 Hz, which is the range of interest. The microphone signals are simultaneously captured and analyzed using the transfer function equations (5), (6), (7) to calculate α .

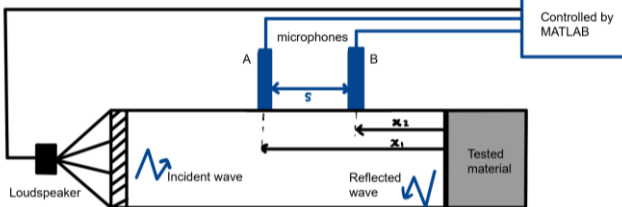


Fig. 12. Layout of the impedance tube. A combination of incident and reflected waves is measured at different positions using microphones A and B. A loudspeaker is positioned at one end of the tube, while the tested material is placed at the opposite end, facilitating measurements of the material's acoustic absorption properties.

To ensure accuracy and minimize random errors, the device was tested three times in an impedance tube. Fig. 6 presents the averaged results. The absorption coefficients peaked at 90 Hz, 310 Hz, and 850 Hz, closely matching the dominant underground noise frequencies. These results confirm the metamaterial's effectiveness in targeting the identified bandgaps. The continuous absorption spectrum shows at least 50% efficiency across a broad range of frequencies and exceeds 95% efficiency at the peak frequencies. As shown in Fig. 6, the measured absorption aligns well with the COMSOL-simulated spectrum, validating the impedance tube design.

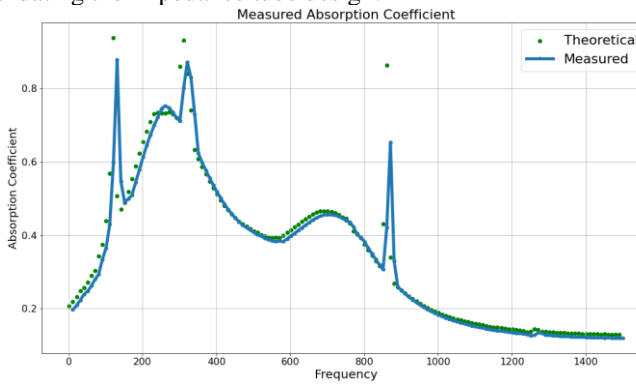


Fig. 13. The absorption spectrum of our product. The peaks correspond to the structure's local resonance frequencies, while the continuous spectrum is attributed to the air local resonance introduced by the perforated plate.

F. Energy transducer

To converting mechanical waves into electrical energy, we select piezoelectric effect. Conventional transducers typically rely on piezoelectric ceramics; however, these ceramics obtain very high resonance frequencies [] that do not match the low-frequency range of the target noise, leading to significant energy loss due to impedance mismatch. To

address this issue, we introduced PVDF (Polyvinylidene fluoride) piezoelectric membranes. PVDF is flexible, allowing for lower and tunable resonance frequencies, and its piezoelectric coefficients are higher compared to those of traditional piezoelectric ceramics.

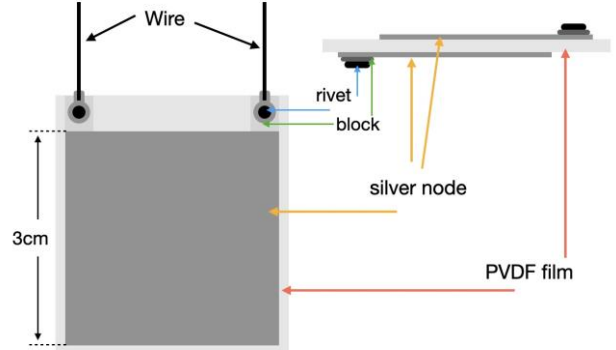


Fig. 14: Structure of PVDF energy transducer

During the transducer fabrication process, according to the figure, silver electrodes are sputtered onto both sides of the polarized PVDF film. Excess electrodes are then removed using acetone or ethanol. Since the membrane is sensitive to heat, which could cause damage, the terminals are fixed onto the membrane using a riveting method instead of soldering. Finally, the membrane is attached to the vertex of the defect as shown in Figure 15.

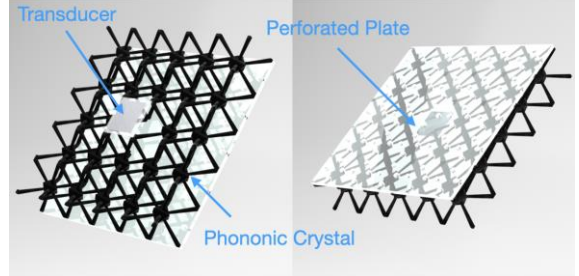


Fig. 15 Structure of the whole device

To evaluate the energy conversion performance, we used a loudspeaker to play recorded noise at approximately 100 dB, with the sound waves vertically incident on the device. The PVDF piezoelectric membranes were connected in parallel to a $1\text{ k}\Omega$ resistor, and the output voltage was measured using an oscilloscope. The average voltage recorded was $2.37 \pm 0.29\text{ V}$. Using this data, the output power P can be calculated as $5.62\text{ mW} \pm 1.37\mu\text{W}$.

III. CONCLUSIONS AND IMPLEMENTATION

Based on our current achievements, we have successfully met the objectives set for the development of our device. By designing unique acoustic metamaterials, we achieved nearly perfect sound absorption (absorption coefficient 0.95) over a broad frequency range, as well as significantly higher power generation capabilities in the milliwatt range compared to similar studies. Additionally, our research leveraged advanced deep learning-based inverse design methods. Due to the high-customizability of our device, we are able to tailor them for various implementations. The London Underground is a case study presented, but we are seeking opportunities for it to be applied in power plants, factories, airports, and other places with noise pollutions.

However, our testing remains at the laboratory stage, and field tests in subway tunnels have yet to be conducted. In future work, we will prioritize in-situ testing to evaluate the

device's power generation and sound absorption performance under real-world conditions. We plan to design a standalone system that includes transducers connected to batteries and charging circuits, allowing the device to be deployed long-term in subway tunnels and factories to simulate actual operational scenarios. This will enable us to assess its long-term power output, stability, and durability, especially in challenging environments with the disruption of other factors including dust, temperature, and etc. We plan to produce 100-300 units for on-site testing in factories or undergrounds, pending TfL's approval.

Moreover, we aim to enhance our design methodology by exploring multi-material acoustic metamaterials with varied density and elastic modulus parameters to further improve energy convert efficiency and reduce production costs. We also plan to develop a deep learning model specifically for predicting sound absorption performance, as time and computational limitations prevented us from completing this step during the current study, relying more on trial-and-error approaches instead. The prototype will then proceed through regulatory approvals and DTC development. The detailed product development and plan of commercialization can be found in Chapter V – ‘Future Plans’.

IV. INTELLECTUAL PROPERTY AND MARKET RESEARCH

A. Market research

The metamaterial market is experiencing rapid growth, with a projected compound annual growth rate (CAGR) of 32.01%. It is expected to expand from \$0.9 billion in 2022 to \$14.5 billion by 2032. The market is dominated by three key sectors: the electromagnetic segment (30% of revenue), antenna and radar (43%), and aerospace (34%) [30]. In contrast, the commercial application of acoustic metamaterials remains relatively untapped, with only a few notable companies such as Acoustic Metamaterial Group Ltd [31] and Sonobex Ltd [32]. Both companies, established within the last decade, originated from university research labs—Hong Kong University of Science and Technology (HKUST) and Loughborough University, respectively. Their services, focused on noise reduction, are business-to-business

such as glass wool, synthetic fibers, and specialized chemicals [34]. These materials, often derived from crude oil, are subject to price volatility, leading to instability in supply for insulation manufacturing [34]. In contrast, our solution uses recycled rubbers like TPU and TPE, which benefit from an established, stable supply chain. This approach not only ensures consistent production but also supports a shift toward more environmentally friendly acoustic insulation by relying solely on renewable and recycled materials.

Our business offers a B2B service focused on industries with high noise levels and potential for energy harvesting. Rather than competing directly with traditional noise-absorbing solutions, our product stands out by converting noise into electricity, creating a unique value proposition in the market. We prioritize sustainability through reuse, renewal, and recycling, aiming to replace unsustainable soundproofing methods with net-zero production processes. Our mission extends beyond innovation—we are committed to promoting safety and addressing the often-overlooked issue of noise pollution, which affects millions globally [35]. Format and save your graphics using a suitable graphics processing program that will allow you to create the images as PostScript (PS), Encapsulated PostScript (.EPS), Tagged Image File Format (.TIFF), Portable Document Format (.PDF), or Portable Network Graphics (.PNG) sizes them, and adjusts the resolution settings. Where possible save your figures as a *vector art* format to stop text in the figures becoming pixelated.

B. Patent research

There are existing patents within the field of acoustic metamaterial energy harvesting but does not intersect with our device.

While increasing attention is being paid to low-frequency sound absorption and acoustic energy harvesting, few studies have integrated these two aspects into a single approach. For sound absorption, conventional metamaterial designs often employ space-coiling structures that rely on coherent wave cancellation [36,37] or use porous materials [38] that dissipate sound energy as heat, both of which fail to effectively capture the energy.

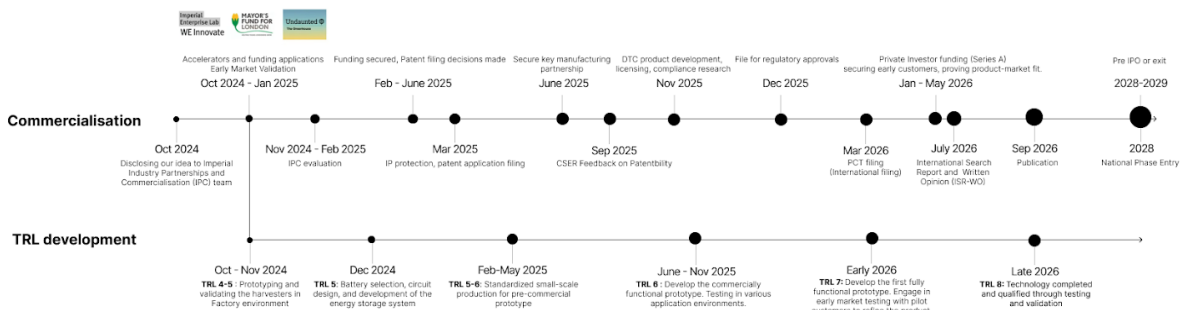


Fig. 16. The Future Timeline for product development in a. Commercialization (Market development and Patenting) and b. TRL (Technology Readiness Level) development.

(B2B) and include the sale of sound-absorbing panels and soundproof chambers [33]. In general, the metamaterial market is rapidly growing, with successful applications in defense and communications. There is a clear trend toward commercializing metamaterials, with limited competition in this emerging, unsaturated market.

Meanwhile, the acoustic insulation market faces significant challenges due to the high cost of raw materials,

For acoustic energy harvesting, common methods use piezoelectric ceramics to convert sound energy [39], but their conversion efficiency is typically very low due to impedance mismatch at low frequencies. (CN113067498B) [40] We use 28mm PVDF composite films with higher piezoelectric coefficient compared to ceramic piezo disc. This contributes to better output performance of nanogenerators and therefore more suitable for energy harvesting [41].

Additionally, individual Helmholtz resonators are often used to capture sound waves [42], with each unit requiring a separate transducer. This setup results in low conversion efficiency, usually in the micro-watt range, and high costs, making it impractical for real-world applications.

The most comparable studies [43] to ours also focus on absorbing and converting train noise; however, they primarily use Helmholtz resonators to capture sound waves and directly drive the transducers, unlike our approach that converts sound waves into mechanical waves and concentrates them. As a result, their conversion efficiency remains low, requiring a greater number of transducers, which significantly suppresses commercialization potential due to increased complexity and cost.

C. Company Exploitations

We have established initial connections with relevant staff at Transport for London (TfL) and are drafting a preliminary collaboration plan, set to be finalized after our report submission. We will join the Net Zero initiative [44] in October 2024 and engage with TfL in November 2024 for a final pitch and plan review. TfL's key priorities for 2024 include promoting carbon neutrality and enhancing the safety of the London Underground. Our solution addresses these goals with an estimated £10 million initial investment, an eight-year payback period, and projected annual savings of £8 million on noise management, totaling £30 million over five years [35]. In addition, we are in discussions with companies in China, including Gree Electric in Guangdong, to explore the potential for field testing and installation in their factories. These discussions are focused on evaluating commercialization opportunities and estimating costs and revenue, though no formal partnerships have been established at this stage.

For the manufacturing and industrial supply of our device, we are in discussions with factories in Guangzhou, China, regarding extrusion molding of PTE and large-scale production of the crystal structure. Additionally, we have engaged with regional sales representatives from Poly K, a supplier of PVDF film, to negotiate pricing and calculate mass production costs. We have already secured a 30% reduction in material costs for our 8-week placement.

V. FUTURE PLANS

The following image outlines our future product and commercial development plans. A detailed, zoomed version can be found in the appendix.

A. Technological perspective

Through the MAD placement, we have advanced to a Technology Readiness Level (TRL) of 3-4 [45], with a lab-validated product. We will allocate £1,000 towards circuit design as mentioned in Chapter III, and finalizing the energy storage method by December. Once the energy storage is defined, we plan to conduct on-site testing to reach TRL 5 by May 2025. The prototype will then proceed through regulatory approvals and DTC development. Upon validation of a commercial prototype (TRL 6), we will work with early market customers to refine the product by late 2025. These devices will be tailored to specific noise environments, with standardized industrial design for production, supported by

funding from accelerator and incubation programs. Full-scale development and qualification for testing will follow once private investor funding is secured, with early customer engagement planned for 2026-2027. Continuous customer feedback and reinvestment of profits will drive ongoing product development.

B. Securing fundings and Commercialization

We plan to apply for the following accelerator and incubation programs: Mayor's Fund for London (Entrepreneur Program) [46] in February 2025, WE Innovate [47] in October 2024, and Undaunted Greenhouse Accelerator [48] in Spring 2025. Our objectives in joining these programs include: 1. Securing funding for patent applications (initial filing and CSER feedback), DTC/DTB product development, commercial consultation, licensing fees, and regulatory approvals. 2. Developing essential soft skills such as customer discovery, IP protection, and funding strategies to address our knowledge gaps in commercializing the product successfully. 3. Accessing mentorship, peer support, and networking opportunities, which will be crucial for connecting with private investors to secure the necessary funding for the next phase. We have chosen these programs specifically because they are either government-funded or affiliated with Imperial College, reducing the risk of intellectual property theft or premature equity exchange.

C. Patent applications

We plan to patent our device following guidance from the Enterprise Division. After conducting initial patent research, we will utilize Imperial's IP consulting services to evaluate the idea. Next, we will submit an Invention Disclosure Form (IDF) detailing the technology. The Imperial IP team will then assess its novelty and commercial potential through an evaluation process, including a prior art search. If deemed viable, we will proceed with filing the patent application. After six months, a Combined Search and Examination Report (CSER) will provide feedback on patentability, with costs rising to £6-7K. If promising, we will move to the international filing stage (PCT) by the 12-month mark, with costs increasing to £12-25K. By months 30-31, we will select countries for National Phase Entry, typically including the UK. The full process usually takes 4-5 years and can cost £35-38K for patents in key markets [49].

Patenting in the UK requires a steady cash flow throughout the process, with initial filing costs estimated at £5-6K, which exceeds our current funds. If external funding is unavailable, we will explore patenting in China, following consultation with Imperial's IPC team. We are fully informed about Imperial's Intellectual Property regulations as students [50]. Patenting in China typically takes 1-3 years from filing to completion. In the event of insufficient funding, we will allocate £800 to secure the patent in China for three years [51].

D. Budgeting the funds

The detailed budget for the £6,000 MAD grant is outlined as follows. This funding will support our activities from October 2024 through February-May 2025 across several key areas to ensure development and market entry are covered:

1. Technical Development (TRL 4-5 to TRL 5-6): This includes costs for prototyping, circuit design, small-scale manufacturing and on-site testing.

2. Market Research: Funds will cover early market analysis and reports to engage with initial customers and adapt the product to meet market demands.
3. Patent Fees: A portion of the budget is reserved for patenting in China, should funding for UK patent filing be insufficient.
4. Miscellaneous Funds: This includes emergency funds and costs related to participating in accelerators and incubation programs..

Budget	
Personal Use	1000
Development Budget	6000
Patent Cost	
Application fee	(380)
Securing for 3 years	(3x100)
Circuit development	
Lab Consumables	(700)
Consulting	(300)
DRL 6 development	
Moulding	(537)
Field rental	(300)
200-300 units	(1038-1557)
Early Market Research	
Customer consulting	(200)
Market Analysis	(300)
Industry Networking	(300)
Digital Marketing for Early Engagement	(200)
	(1000)
Miscellaneous Costs	
Unforeseen Expenses	(926-1000)

Unit cost calculation excluding fixed costs:	
Raw material	Cost (in RMB)
Pvdf film	1500/38
	17
Ports	0.03 x 2
PET film	0.0065
Wires	0.021
Rivets	0.00675 x 2
Alcohol	0.06
Acrylic board	2.67
TPE	1.42
Manufacturing	
Extrusion Molding	5
Cutting and drilling	2
Labor	0.8 x 25
Transportation	
Transport by truck	0.09
Total	48.341
Total in GBP	5.19 GBP

Fig. 17. Tables of a. detailed budgeting of MAD's funds, and b. unit cost calculations. (Detail see Appendix. A)

With the allocated funds as in the table, we aim to achieve several key milestones: establishing a small-scale manufacturing partnership, advancing our product to TRL 5-6 for compliance and regulatory research, DTC development, conducting early market analysis, and positioning within industrial networks. Additionally, we plan to secure grants for further development and patent filing. Without the MAD funding, we would not be able to transition our lab-ready product to early-stage commercialization—an essential step in attracting future investors.

By 2029, we envision our product reaching TRL 9 (market readiness), with streamlined operations that maximize profitability and prepare the business for potential acquisition or public investment. We also plan to secure our patent through successful National Phase Entry.

REFERENCES

- [1] T. Munzel, T. Gori, W. Babisch, and M. Basner, "Cardiovascular effects of environmental noise exposure," *European Heart Journal*, vol. 35, no. 13, pp. 829–836, Mar. 2014, doi: <https://doi.org/10.1093/euroheartj/ehu030>.
- [2] A. Dinno, C. Powell, and M. M. King, "A Study of Riders' Noise Exposure on Bay Area Rapid Transit Trains," *Journal of Urban Health*, vol. 88, no. 1, pp. 1–13, Jan. 2011, doi: <https://doi.org/10.1007/s11524-010-9501-1>.
- [3] Transport for London, "Reducing noise & vibration," *Transport for London*. <https://tfl.gov.uk/corporate/about-tfl/reducing-noise-and-vibration>
- [4] P. Hatziantoniou and J. Mourjopoulos, "Generalized fractional-octave smoothing of audio and acoustic responses," *J. Audio Eng. Soc.* , vol. 48, pp. 259-280, 2000.
- [5] V. G. Veselago, "The electrodynamics of substances with simultaneously negative values of μ and ϵ ," *Soviet Phys. Usp.,* vol. 10, no. 4, pp. 509-514, 1968.
- [6] J. B. Pendry, A. J. Holden, D. J. Robbins, et al., "Magnetism from conductors and enhanced nonlinear phenomena," *IEEE Trans. Microwave Theory Tech.,* vol. 47, no. 11, pp. 2075-2084, 1999.
- [7] Z. Liu, X. Zhang, Y. Mao, Y. Y. Zhu, Z. Yang, C. T. Chan, and P. Sheng, "Locally resonant sonic materials," *Science,* vol. 289, no. 5485, pp. 1734-1736, Sep. 8, 2000, doi: 10.1126/science.289.5485.1734.
- [8] J. Chen, J. Xiao, D. Lisevych, et al., "Deep-subwavelength control of acoustic waves in an ultra-compact metasurface lens," *Nat. Commun.* , vol. 9, no. 4920, 2018, doi: 10.1038/s41467-018-07315-6.
- [9] L. Xiang, G. Wang, and C. Zhu, "Controlling sound transmission by space-coiling fractal acoustic metamaterials with broadband on the subwavelength scale," *Appl. Acoust.* , vol. 188, 108585, 2022, doi: 10.1016/j.apacoust.2021.108585.
- [10] S. A. Cummer and D. Schurig, "One path to acoustic cloaking," *New J. Phys.* , vol. 9, p. 45, 2007.
- [11] G. Ma and P. Sheng, "Acoustic metamaterials: From local resonances to broad horizons," *Sci. Adv.* , vol. 2, e1501595, 2016, doi: 10.1126/sciadv.1501595.
- [12] M. Yang, C. Meng, C. Fu, Y. Li, Z. Yang, and P. Sheng, "Subwavelength total acoustic absorption with degenerate resonators," *ArXiv*, 2015, doi: 10.1063/1.4930944.
- [13] K. Grilec, G. Marić, and K. Miloš, "Aluminium foams in the design of transport means," *Promet-Traffic & Transportation,* vol. 24, no. 4, Aug. 2012, doi: 10.7307/ptt.v24i4.437.
- [14] J. Liu, Y. Yu, D. Zhao, et al., "Theoretical study of two-dimensional phononic crystals viscoelasticity based on fractional derivative models," *J. Phys. D: Appl. Phys.,* vol. 41, 065503, 2008.
- [15] S. Guenneau, C. G. Poulton, and A. B. Movchan, "Oblique propagation of electromagnetic and elastic waves for an array of cylindrical fibres," *Proc. R. Soc. Lond. A*, vol. 459, pp. 2215-2263, 2003.
- [16] Bloch, F. Zeitschrift fur Physik, 52, 555-600.1928
- [17] S. Guenneau, C. G. Poulton, and A. B. Movchan, "Oblique propagation of electromagnetic and elastic waves for an array of cylindrical fibres," *Proc. R. Soc. Lond. A*, vol. 459, pp. 2215-2263, 2003.
- [18] Tirth S, Tunneling in the Brillouin zone: Theory of backscattering in valley Hall edge channels, *Phys. Rev. B* 104, 235431 –2021
- [19] Liu Z, Zhang X, Mao Y, Zhu YY, Yang Z, Chan CT, Sheng P. Locally resonant sonic materials. *Science*. 2000 Sep 8;289(5485):1734-6.
- [20] Sattar M E, Ali D, Mohammad A, Topology optimization of additive-manufactured metamaterial structures: A review focused on multi-material types, *Forces in Mechanics*, Volume 7,2022.
- [21] Mohsen P, Habib Y R, Hadi V, EEG-based classification of individuals with neuropsychiatric disorders using deep neural networks: A systematic review of current status and future directions, *Computer Methods and Programs in Biomedicine*, Volume 240, 2023,
- [22] A. Asperti and M. Trentin, "Balancing Reconstruction Error and Kullback-Leibler Divergence in Variational Autoencoders," in *IEEE Access*, vol. 8, pp. 199440-199448, 2020, doi: 10.1109/ACCESS.2020.3034828.
- [23] X. Li, S. Ding, X. Wang, W. Zhai, et al., "Recipe for simultaneously achieving customizable sound absorption and mechanical properties in lattice structures," *Adv. Mater. Technol.* , Sep. 2024, doi: 10.1002/admt.202400517.
- [24] Li, X., Chua, J. W., Yu, X., Li, Z., Zhao, M., Wang, Z., & Zhai, W. (2023). 3D-Printed Lattice Structures for Sound Absorption: Current Progress, Mechanisms and Models, Structural-Property Relationships, and Future Outlook. *Advanced Science*, 11(4), 2305232.
- [25] Brüel & Kjær , "Product Data: Impedance Tube Kit (50 Hz – 6.4 kHz) Type 4206, Impedance Tube Kit (100 Hz – 3.2 kHz) Type 4206-A, Transmission Loss Tube Kit (50 Hz – 6.4 kHz) Type 4206-T (bp1039)," 2016.
- [26] M. Suhanek, K. Jambrošić, and H. Domitrović, "Student project of building an impedance tube," *The Journal of the Acoustical Society of America*, vol. 123, no. 5, June 2008, DOI: 10.1121/1.2934823.
- [27] S. Deshpande, "Development of a Low-Cost Impedance Tube to Measure Acoustic Absorption and Transmission Loss of Materials," in *Proc. American Society for Engineering Education Annual Conference*, Indianapolis, IN, June 2014, DOI: 10.18260/1-2--20308.
- [28] A. Ando, "Resonance characteristics derived by structural design of thermally stable piezoelectric ceramics," Murata Mfg. Co., Ltd., Nagaokakyo, Kyoto, Japan.
- [29] S. Sepehri, M. M. Mashhadi, and M. M. S. Fakhraabadi, "Wave propagation in fractionally damped nonlinear phononic crystals," *Nonlinear Dyn*, vol. 110, pp. 1683–1708, 2022, DOI: 10.1007/s11071-022-07704-z.
- [30] Precedence Research, "Metamaterials Market Size To Attain USD 14.5 Bn By 2032," www.precedenceresearch.com, Dec. 2022. <https://www.precedenceresearch.com/metamaterials-market>
- [31] Acoustic Metamaterial Group, "Home - AMG," *AMG - Redefining Silence*, 2020. <https://metacoust.com/> (accessed Sep. 20, 2024).
- [32] Merford, "Sonobex next generation noise control," *Merford.com*, Jan. 20, 2021. <https://www.merford.com/en/news/sonobex-next-generation-noise-control> (accessed Sep. 20, 2024).

- [33] Acoustic Metamaterial Group, "Products - AMG," *AMG - Redefining Silence*, Nov. 15, 2022. <https://metacoust.com/products/> (accessed Sep. 20, 2024).
- [34] Market and Markets, "Acoustic Insulation Market, Industry Size Forecast," *MarketsandMarkets*, Aug. 2024. <https://www.marketsandmarkets.com/Market-Reports/acoustic-insulation-market-41399747.html>
- [35] B. News, "London Underground: Nearly £30m spent on noise cuts over five years," *Bbc.com*, Jul. 30, 2024. <https://www.bbc.com/news/articles/cd1r70xvk6vo> (accessed Sep. 20, 2024).
- [36] P. Hu, J. Zhao, H. Liu, X. Zhang, G. Zhang, and H. Yao, "Low-frequency sound-insulation performance of labyrinth-type Helmholtz and thin-film compound acoustic metamaterial," **Air*
- [37] I. Lee, I. Han, and G. Yoon, "Compact acoustic metamaterials based on azimuthal labyrinthine channels for broadband low-frequency soundproofing and ventilation," **Dept. of Manufacturing Systems and Design Engineering, Seoul National Univ. of Science and Technology, Seoul, Republic of Korea**.
- [38] Y. Zhang, C. Wu, N. Li, T. Liu, L. Wang, and Y. Huang, "Ventilated low-frequency sound absorber based on Helmholtz acoustic metamaterial," **Chongqing Key Laboratory of Interface Physics in Energy Conversion, College of Physics, Chongqing University, China.**
- [39] S. Mallesh, J. Hwang, H. Choi, D.-J. Hong, C. Seok, B. Kwak, S.-Y. Lee, and Y. Nam, "Advanced acoustic design: 3D printed thermoplastic folded core sandwich structures with porous materials and microperforations for enhanced sound absorption," **Compos. Struct.**, vol. 345, 118371, 2024.
- [40] Y. Pan, J. Zhao, Q. Li, and Z. Zhang, "Multilayer plate energy harvesting structure based on defect state acoustic metamaterial," Dec. 16, 2022 Accessed: Sep. 15, 2022. [Online]. Available: <https://patents.google.com/patent/CN113067498B/en?oq=CN113067498B>
- [41] L. Lu, W. Ding, J. Liu, and B. Yang, "Flexible PVDF based piezoelectric nanogenerators," *Nano Energy*, vol. 78, p. 105251, Dec. 2020, doi: <https://doi.org/10.1016/j.nanoen.2020.105251>.
- [42] A. I. Komkin, M. A. Mironov, and A. I. Bykov, "Sound absorption by a Helmholtz resonator," *Bauman State Technical Univ., Moscow, Russia, Andreev Acoustics Institute, Moscow, Russia*, 2016.
- [43] J. Zuo, L. Dong, F. Yang, Z. Guo, T. Wang, and L. Zuo, "Energy harvesting solutions for railway transportation: A comprehensive review," **Dept. of Mechanical Engineering**, authors affiliated with various institutions.
- [44] T. for L. | E. J. Matters, "Open innovation," *Transport for London*. <https://tfl.gov.uk/info-for/business-and-advertisers/open-innovation>
- [45] C. Manning, "Technology Readiness Levels - NASA," *NASA*, Sep. 27, 2023. <https://www.nasa.gov/directorates/somd/space-communications-navigation-program/technology-readiness-levels/>
- [46] Mayor's Fund for London, "Mayor's Entrepreneur Competition Programme," *Mayor's Fund for London*, May 17, 2024. <https://www.mayorsfundforlondon.org.uk/employability-skills/mayors-entrepreneur-competition/the-programme/> (accessed Sep. 20, 2024).
- [47] Imperial Enterprise , "WE Innovate | Imperial Enterprise Lab," *Imperial Enterprise Lab*, Sep. 16, 2024. <https://www.imperialenteriselab.com/programmes/we-innovate/> (accessed Sep. 20, 2024).
- [48] Undaunted, "The Greenhouse - Undaunted," *Undaunted*, Jun. 04, 2024. <https://undaunted-hq.org/programmes/the-greenhouse/> (accessed Sep. 20, 2024).
- [49] The Industry Partnerships and Commercialisation (IPC) team, "Redirecting," *Imperial.ac.uk*, 2024. [https://www.imperial.ac.uk/media-access/internal/?folder=administration-and-support-services/enterprise-office/internal&filename=IPC-Guide_version-1_2_November-2020-\(Protected\).pdf](https://www.imperial.ac.uk/media-access/internal/?folder=administration-and-support-services/enterprise-office/internal&filename=IPC-Guide_version-1_2_November-2020-(Protected).pdf) (accessed Sep. 20, 2024).
- [50] Director of the Research Office, "Policy Title INTELLECTUAL PROPERTY POLICY Version 1 -Public Access Reference ROP/07 Effective Date of Policy," Aug. 2023. Accessed: Sep. 20, 2024. [Online]. Available: <https://www.imperial.ac.uk/media/imperial-college/research-and-innovation/research-office/public/Intellectual-Property-Policy-ROP-07-Public-Access.pdf>
- [51] European Commission, "Patent protection cost in China," *IP Helpdesk*, 2023. https://intellectual-property-helpdesk.ec.europa.eu/patent-protection-cost-china_en (accessed Sep. 20, 2024).

APPENDICES

A. Budgeting Calculations

Budget	
Personal Use	1000
Development Budget	6000
Patent Cost	
Application fee	(380)
Securing for 3 years	(3x100)
Circuit development	
Lab Consumables	(700)
Consulting	(300)
DRL 6 development	
Moulding	(537)
Field rental	(300)
200-300 units	(1038 -1557)
Early Market Research	
Customer consulting	(200)
Market Analysis	(300)
Industry Networking	(300)
Digital Marketing for Early Engagement	(200)
	(1000)
Miscellaneous Costs	
Unforeseen Expenses	(926-1000)

Unit cost calculation excluding fixed costs:

Raw material	Cost (in RMB)
Pvdf film	1500/88
	17
Ports	0.03 x 2
PET film	0.0065
Wires	0.021
Rivets	0.00675 x 2
Alcohol	0.06
Acrylic board	2.67
TPE	1.42
Manufacturing	
Extrusion Molding	5
Cutting and drilling	2
Labor	0.8 x 25
Transportation	
Transport by truck	0.09
Total	48.341
Total in GBP	5.19 GPB

1. The Pvdf film is sold at 1500 RMB per A4 paper size (29.7 x 21cm), one unit require 2.5x2.5 cm, so one film is capable of manufacturing 88 units.
2. The mould for extrusion moulding typically cost around 200-1000 pound according to the factory we contacted. The unit cost is based on the cost being split equally for each unit, around 20-100 RMB per unit. The unit cost decreases with the increase in number of units manufactured,
3. Each crystal structure has volume of 39.696 cm^3, and the density of TPE is usually 0.8-1.2 g/cm^3(R), the total raw material required is 47.63g. The price of 1kg TPE is around 30 RMB, the total raw material cost is therefore 1.42 RMB.
4. The labor cost is calculated based on 0.5 hours spent on the assembly of the center mechanical vibration converter, and 0.12 hours spent for molding and cutting, and 0.18 hours spent for assembly. The hourly rate of labor is average 25 RMB.
5. The transportation of 1M^2 from the factory to our field experiment location is calculated by around 100 RMB per 1m^3. One unit occupies 0.15 x 0.15 x 0.04 = 0.0009 m^3. The total price is calculated at 0.09 RMB.
6. The currency exchange rate between GBP and CNY is around 9.3 RMB = 1 GBP.

B. Future Development Timeline (Vertical)

